Sustainable Production through Advanced Manufacturing, Intelligent Automation and Work Integrated Learning, J. Andersson et al. (Eds.)

doi:10.3233/ATDE240152

Study of Pulsed Laser Beam Welding of Nickel-Based Superalloy G27

Achmad ARIASETA[a,c,1], Dario PICK[a], Joel ANDERSSON[a], and Olanrewaju OJO[b]
[a] *Department of Engineering Science, University West, SE-46186 Trollhättan, Sweden*
[b] *Department of Mechanical Engineering, University of Manitoba, Winnipeg, MB R3T 5V6, Canada*
[c] *Department of Metallurgical Engineering, Faculty of Mining and Petroleum Engineering, Institut Teknologi Bandung, Jl. Ganesha 10, Bandung 40132, Indonesia*
ORCiD ID: Achmad Ariaseta https://orcid.org/0000-0002-9520-0456

Abstract. The influence of pulsed laser beam welding (LBW) parameters on the weld geometry and imperfections of a new nickel-based superalloy called G27 was studied by a statistical design of experiment, and the microstructures of the weld fusion zone (FZ) of the pulsed laser beam-welded G27 were characterized. No evidence of cracks is found in the FZ and heat-affected zone (HAZ). Other weld imperfections, such as undercut and underfill, were also hardly observed. The pulse factor significantly influenced all the responses, i.e., minimum weld width (Wm), root excess weld metal, and average pore diameter, whereas welding travel speed significantly influenced Wm and root excess weld metal. Power and interaction between pulse frequency*pulse factor were statistically significant in influencing the root excess weld metal and average pore diameter, respectively. The pulse frequency and interactions between power*travel speed, power*pulse factor, power*pulse frequency, travel speed*pulse factor, and travel speed*pulse frequency did not significantly influence any response. Microsegregation pattern that occurs during weld solidification leads to the formation of Nb-rich MC carbides and Nb-rich Laves phase as the major secondary phase constituents in the FZ of as-welded G27. The presence of brittle Laves phase requires careful consideration when developing suitable post-weld heat treatment of G27.

Keywords. G27 superalloy, pulsed laser beam welding, weld geometry, microstructure

1. Introduction

G27 is a new wrought nickel-based superalloy strengthened by γ' that has been developed for aerospace applications to achieve comparable mechanical properties to alloys such as Waspaloy in terms of crack growth during dwell fatigue, notch ductility, stress rupture, high-temperature strength, and microstructural stability [1]. This new alloy is intended for elevated-temperature applications such as the hot structural components of jet engines with a service temperature that can be as high as 760°C. G27 is designed to be Co-free with a substantially lower raw material cost than Waspaloy.

[1] Corresponding Author: Achmad Ariaseta, achmad.ariaseta@hv.se

In the aerospace industry, welding is extensively utilized to fabricate hot sections of jet engines. Utilizing welding to join smaller superalloys, rather than casting a single large component, is believed to offer several notable advantages, including improved design flexibility, which facilitates the joining of cast (geometrically intricate) alloys with wrought (high-strength) alloys or even combining completely different superalloys. Moreover, this technique reduces the overall weight of the parts, enhancing fuel efficiency and consequently lessening the environmental impact.

Pulsed laser beam welding remains an appealing joining method to rapidly produce narrow, deep penetrating welds with minimal heat input, ensuring high reliability and productivity. Obtaining a sound and high-quality pulsed laser-beam weld that aligns with stringent weld quality standards within the aerospace sector regarding weld geometry and imperfections is critical. Also, understanding the fusion zone (FZ) microstructure formed during weld solidification is paramount, given that the rapid solidification in the weld during cooling typically leads to elemental microsegregation, which often results in the formation of harmful secondary intermetallic microconstituents that may impact the weld's mechanical properties and integrity. Understanding the FZ microstructure is also crucial for developing an appropriate post-weld heat treatment (PWHT) strategy for the alloy. Thus, this work aims to study the effect of pulsed laser beam welding parameters on the weld geometry and imperfections when welding G27 superalloy and to characterize the FZ microstructure in the as-welded condition.

2. Experimental procedures

2.1. Material and welding

As-hot-rolled 300 x 30 x 4.2 mm^3 G27 superalloy plates with the chemical composition (in wt%) shown in Table 1 were used for the bead-on plate weld runs using the robotic pulsed laser beam welding process. High-purity argon gas (99.99%) was used as shielding gas, with a 10 L/min flow rate.

Table 1. Chemical compositions of G27 (wt%) used in the present study.

Element	Ni	Al	Ti	Nb	S	Cr	Ta	V	Zr	Mo	Co
wt%	Bal.	1.90	1.88	3.70	0.001	15.11	<0.02	0.1	0.03	4.02	0.18

Element (cont.)	Si	Mn	C	P	Cu	Ca	Mg
wt% (cont.)	0.06	0.06	0.028	0.007	0.04	<0.0005	0.0034

Element (cont.)	B	N	O	Fe
wt% (cont.)	0.005	0.006	0.001	15.00

2.2. Statistical design of experiment

The DOE used to study the effect of pulsed laser beam welding parameters on the weld geometry and imperfections in this work was based on a two-level full factorial design with four factors, i.e., laser power, travel speed, pulse factor, and pulse frequency. Pulse factor is defined as a ratio between maximum and minimum laser power. Three center

points, i.e., Samples 17, 8, and 19, were added, resulting in 19 experiments. The levels defined for the parameters of pulsed laser beam welding with their notations, units, and levels are shown in Table 2. The ranges of welding parameters were carefully chosen to produce a full penetration weld without burning through the plate. The levels of factors were represented on a coded scale. For example, the 2230, 2330, and 2430 W power levels are coded −1, 0, and 1, respectively. The same codification goes for the other factors. After welding the samples, the typical features of weld geometry and imperfections specified in AWS D17.1M:2010 [2] as the responses were measured in the as-welded plate, i.e., root excess weld metal and average pore diameter. Face excess weld metal, underfill, and undercut were hardly observed in all DOE samples. In addition, measurements on minimum weld width (Wm) and cracks were also carried out. Then, the results were input into Modde software (MODDE 12, Umetrics, Umeå, Sweden) for the DOE analysis.

Table 2. Pulsed laser beam welding parameters and their levels used in this work.

No.	Pulsed beam laser welding parameters	Units	Process parameter levels		
			-1	0	1
1	Laser power (P)	W	2230	2330	2430
2	Travel speed (v_w)	mm/s	7.33	8.33	9.33
3	Pulse factor (f_p)	-	73	83	93
4	Pulse frequency (PF)	Hz	1.5	2	2.5

2.3. Measurement of weld geometry and imperfections

Five transverse cross-sections were cut at the center of the welded plates. The mounted cross-sections were then prepared by standard metallographic procedure through multistep grinding with the grit sizes down to 52 μm, followed by three polishing steps with diamond suspensions with the sizes down to 0.02 μm colloidal silica (SiO_2). Electrolytic etching using 10% oxalic acid at 2 V was performed to reveal the bead geometry. Macrographs of the cross-sections were taken from the etched samples using an optical microscope (OM) to get precise measurements of Wm and root excess weld metal, where the values were averaged from five cross-sections.

The average pore diameter was measured using OM micrographs taken from an as-polished sample. ImageJ software was utilized to measure the pore diameter of a welded plate in the whole FZ area of five cross-sections. The pore diameters of five cross-sections of one welded plate were then averaged to obtain the average pore diameter.

The measured root excess weld metal and average pore diameter obtained from the whole of the DOE runs were compared with the maximum acceptable limit stipulated in AWS D17.1M:2010 [2]. It is essential to highlight that the AWS D17.1M:2010 standard does not delineate a specific value for Wm. Consequently, 1.5 mm was adopted as the minimum acceptable limit for aerospace applications for Wm [3].

2.4. Microstructural characterization

The DOE sample used for microstructural characterization was the sample that exhibited the lowest level of root excess weld metal, smallest average pore diameter, and minimum

weld width larger than 1.5 mm. The microstructural examination of the as-welded sample was carried out initially by using OM. A more detailed microstructural examination was then carried out using a ZEISS Gemini field emission scanning electron microscope (FEG-SEM), which was equipped with both Oxford AZtec energy-dispersive (EDS) and Symmetry S2 electron backscatter diffraction (EBSD) detectors.

3. Results and discussion

3.1. Influence of pulsed laser beam welding parameters on the weld geometry and imperfections

All measured DOE responses for Samples 1 to 19 are graphically presented in Figure 1, extracted directly from Table 3. No cracks are found in the FZ and HAZ of all welded samples. The center points for all DOE responses, namely Samples 17 through 19, exhibited reasonably similar values. This convergence is explicitly reflected in the calculated reproducibility values of 0.797, 0.890, and 0.792 for Wm, root excess weld metal, and pore diameter, respectively. Note that a reproducibility value higher than 0.5 suggests good reproducibility [4]. Among the 19 DOE runs conducted, only six met the Wm requirement of 1.5 mm, while the remaining runs failed to achieve a larger Wm, with the average Wm measured at about 0.8 mm. As for root excess weld metal and average pore diameter, all DOE runs produced welds with values below the maximum acceptable limit for both responses as stipulated in AWS D17.1 M:2010 for aerospace applications [2].

The analysis carried out in Modde modeled the responses of the Wm, root excess weld metal, and average pore diameter of the 19 samples to know which parameters strongly influenced the responses and whether there were any substantial interactions among these parameters. Hence, the regression coefficients of each factor and the interaction of factors along their 95% confidence interval are plotted in Figure 2. The factors demonstrating statistical significance (p-value < 0.05) are indicated with a green marker, whereas those that are not statistically significant (p-value ≥ 0.05) and have confidence intervals that include zero are denoted with a red marker. Figure 2 shows that the pulse factor significantly influenced all the responses, whereas welding travel speed significantly influenced Wm and root excess weld metal. Power and interaction pulse frequency*pulse factor were statistically significant in influencing the root excess weld metal and average pore diameter, respectively. The pulse frequency and interactions between power*travel speed, power*pulse factor, power*pulse frequency, travel speed*pulse factor, and travel speed*pulse frequency did not significantly influence any response.

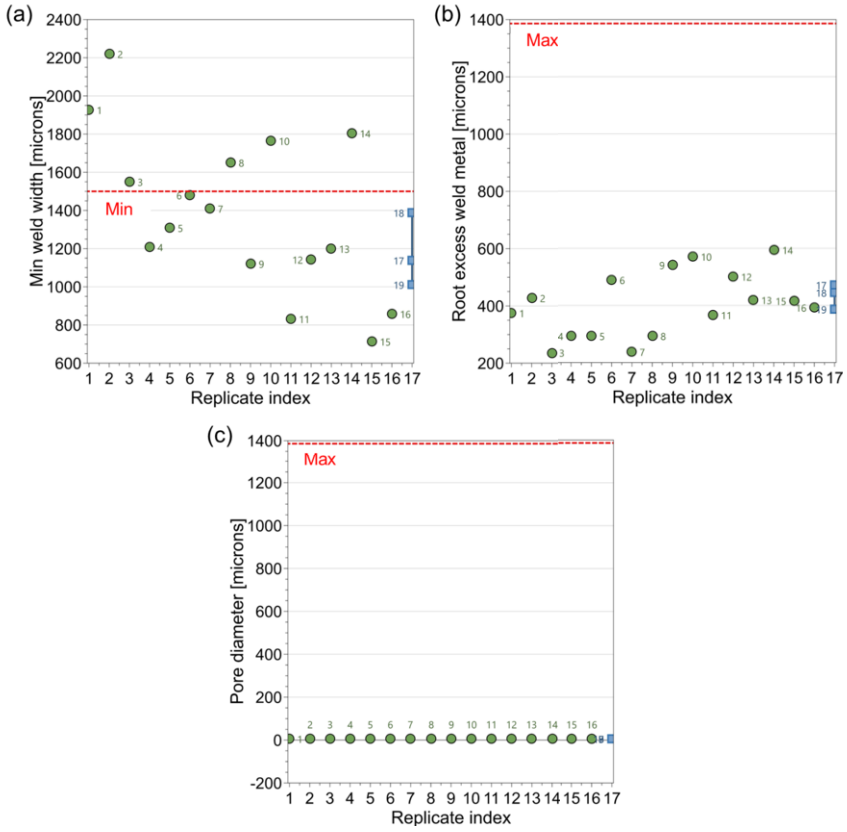

Figure 1. Measured responses of pulsed laser beam welded samples (samples with varied parameters are in green, while replicates are in blue); (a) Wm, (b) root excess weld metal, and (b) average pore diameter.

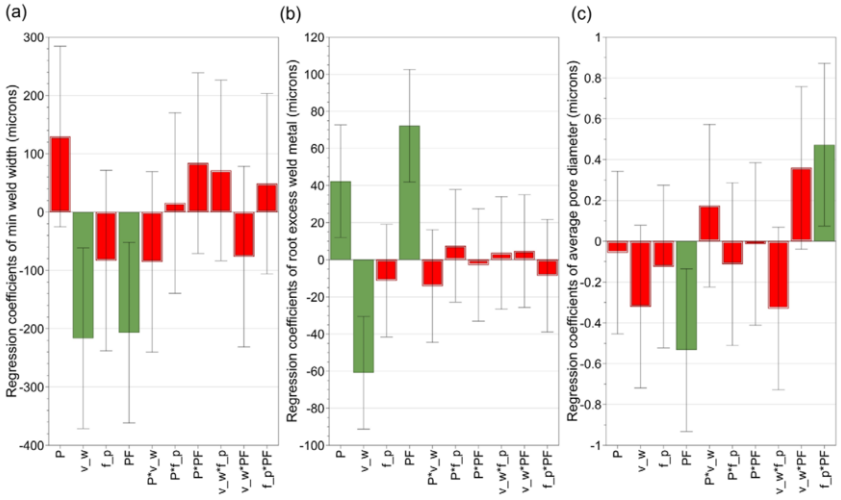

Figure 2. Regression coefficients of factors and interaction of factors influencing (a) Wm, (b) root excess weld metal, and (b) average pore diameter (green bars indicate significant factors, while red bars indicate non-significant factors).

Table 3. Full factorial design of pulsed laser beam welding and the measured responses.

Experiment no.	Power (W)	Travel speed (mm/s)	Pulse frequency (Hz)	Pulse factor	Wm (μm)	Root excess weld metal (μm)	Average pore diameter (μm)
1	2230	7.33	73	1,5	1.926	0.374	0.0077
2	2430	7.33	73	1,5	2.222	0.428	0.0071
3	2230	9.33	73	1,5	1.549	0.236	0.0071
4	2430	9.33	73	1,5	1.207	0.294	0.0074
5	2230	7.33	93	1,5	1.308	0.294	0.0077
6	2430	7.33	93	1,5	1.48	0.488	0.0072
7	2230	9.33	93	1,5	1.412	0.237	0.0046
8	2430	9.33	93	1,5	1.649	0.292	0.0052
9	2230	7.33	73	2,5	1.119	0.541	0.0052
10	2430	7.33	73	2,5	1.766	0.571	0.0053
11	2230	9.33	73	2,5	0.832	0.365	0.0051
12	2430	9.33	73	2,5	1.143	0.502	0.0058
13	2230	7.33	93	2,5	1.202	0.419	0.0064
14	2430	7.33	93	2,5	1.806	0.593	0.0057
15	2230	9.33	93	2,5	0.714	0.416	0.0063
16	2430	9.33	93	2,5	0.86	0.392	0.0057
17	2330	8.33	83	2	1.137	0.471	0.0055
18	2330	8.33	83	2	1.39	0.446	0.0056
19	2330	8.33	83	2	1.011	0.387	0.0050

3.2. Base metal microstructure

Figure 3(a) shows an SEM backscatter electron (BSE) image of the G27 base metal microstructure, revealing a heavily deformed γ matrix with relatively coarse (Nb, Ti)C-type carbide. In high magnification, γ' precipitates of about 10 nm or less are observed as they are dispersed uniformly throughout the microstructure.

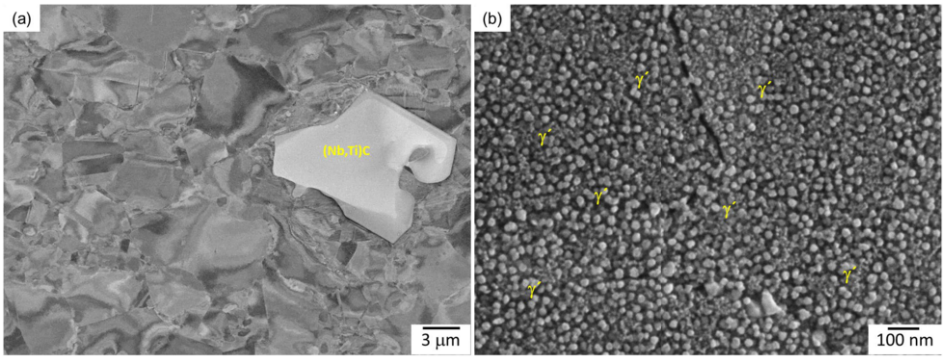

Figure 3. (a) low-magnification SEM BSE image of as-received G27Wm, (b) high-magnification SEM in-lens image that shows fine γ' precipitates throughout the microstructure.

3.3. Fusion zone microstructure

Figure 4 shows an OM micrograph of the FZ microstructure of as-welded G27, showing a cellular dendritic microstructure. The average secondary dendrite arm spacing (SDAS) in the FZ was approximately 4.9 μm, suggesting a rapid cooling rate occurs during the weld FZ solidification. The rapid cooling rate would substantially limit the solute diffusion within the dendrite. Thus, assuming there is no back diffusion in the solidified solid during weld solidification is plausible. Furthermore, DuPont et al. [5] reported that the diffusion of substitutional elements is negligible within the austenitic matrix during the weld solidification upon fusion welding.

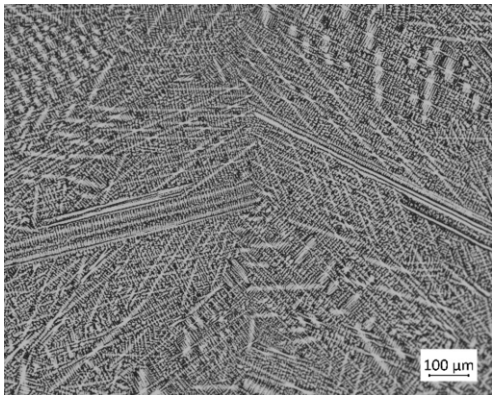

Figure 4. OM micrograph of the FZ microstructure of as-welded G27

The average chemical compositions of at least 20 points taken from the center of the dendrite core close to the fusion boundary were obtained using SEM-EDS and are shown in Table 4. By utilizing this data, the distribution or partition coefficient (k) for the alloying elements was determined, where the k-values describe the direction and degree of microsegregation during the weld solidification. Assuming equilibrium conditions, negligible undercooling at the dendrite tips, and no back-diffusion in the solid, the initial solidification commences with the formation of the dendrite core, having a composition of kC0. C_0 represents the alloy's nominal composition, while k denotes the equilibrium partition coefficient.

As shown in Table 4, both Nb and Ti exhibit k values significantly below unity, indicating a pronounced tendency for these elements to be rejected into the interdendritic liquid during weld solidification. Molybdenum (Mo), Al., and Cr also prefer to segregate into the interdendritic regions, although to a lesser extent than observed with Nb and Ti. Conversely, Ni and Fe exhibit k values exceeding unity, indicating their preference for selective partition into the dendrite core. Through a comparative analysis of the k values determined in this work with those documented in existing literature [6-8] for various commercial Ni-based superalloys listed in Table 4, it becomes evident that the microsegregation characteristics of the major alloying elements in G27 align with the patterns observed in other superalloys, where Nb, Ti, and Mo typically are strongly rejected into the interdendritic liquid, while Ni, Cr, and Fe tend to partition within the dendrite core.

Table 4. The chemical composition of the center of the dendrite core (wt%) determined by SEM-EDS analysis and calculated partition coefficients (k) of the main alloying elements.

Element	Al	Ti	Cr	Co	Ni	Nb	Mo
wt%	1.9	1.88	15.11	15	58	3.7	4.02
k, G27	1.70	1.69	13.45	14.28	62.81	2.68	3.28
Standard deviation of k, G27	0.81	0.56	0.93	1.03	1.09	0.40	0.78
k, alloy 718 [6]	1	0.63	1.03	1.04	1	0.48	0.82
k, ATI 718Plus [7]	1.1	0.7	1.1	1.1	1	0.5	0.9
k, IN 738 LC [8]	0.92	0.69	0.98	-	1.03	0.58	-

Owing to the inherent challenges in accurately quantifying light elements such as C and B using SEM-EDS, their respective k values could not be determined reliably. Additionally, it is worth acknowledging that substantial back-diffusion of interstitial elements can occur during the solidification of welds. However, Knorovsky et al. [9] suggested a k value of approximately 0.2 for C in alloy similar to Alloy 625, indicating its tendency to be rejected into the interdendritic liquid during solidification. Furthermore, Thompson et al. [10] experimentally confirmed the segregation of C into the interdendritic region in another Ni-based superalloy, Alloy 718, utilizing Auger electron spectroscopy. The Ni-X binary phase diagram also implies that the k values for C and B in Ni are below unity. Thus, it is plausible to infer that C and B atoms exhibit extensive segregation into the interdendritic liquid during the solidification of G27 welds. It is important to note that the k values are not necessarily constant throughout the solidification process; however, they effectively elucidate the formation of secondary phase constituents.

Figure 5(a) shows a low-magnification SEM BSE image that reveals the discrete distribution of secondary phase constituents in the interdendritic regions of the FZ. Two major types of secondary phases are observed, as shown in Figure 5(b). The first is irregularly shaped, whereas the second shows blocky and rod-like shapes. Their morphologies and Nb-rich composition obtained by SEM-EDS analysis (Table 5) indicate that these secondary phase constituents are Laves phase and MC-type carbides.

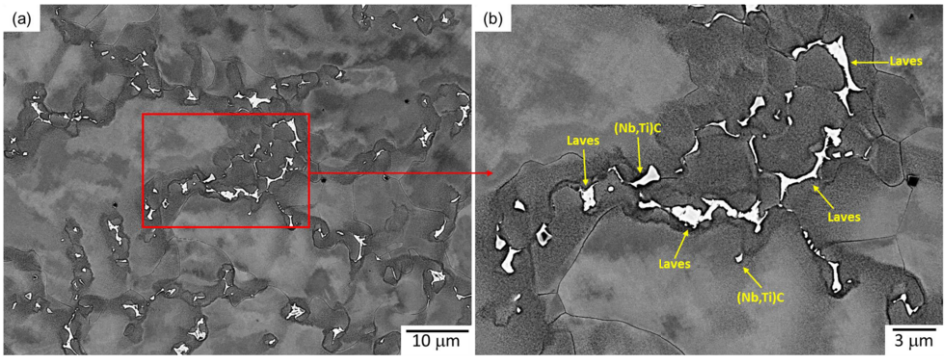

Figure 5. (a) low-magnification SEM BSE image of FZ of as-welded G27, (b) high-magnification of the area highlighted by a red box in (a) that shows Laves phase and Nb-rich MC carbides in the interdendritic region.

Table 5. Semi-quantitative SEM-EDS analysis on secondary phase constituents (wt%) in the FZ.

Particle	Al	Si	Ti	Cr	Fe	Ni	Zr	Nb	Mo
Laves	0.8	0.4	2.6	12.6	10.2	43.2	2.2	20.4	7.6
(Nb,Ti)C	0.7	0.1	11.2	4.1	2.2	6.0	0.5	69.0	6.2

EBSD point analysis was then performed on the secondary phase constituents between the dendrites. Three phases were included in the EBSD phase acquisition, i.e., Ni-superalloy (Ni-matrix), NbC, and $MgZn_2$ (hexagonal C14 Laves phase). $MgZn_2$ was added in the phase acquisition because the Nb-rich Laves phase that forms in superalloys as a solidification product is C14-type with a hexagonal close-packed structure. This analysis used the 'Optimized BD' (formerly known as 'TKD optimized') in current AZtec EBSD software, which maximizes indexing speed and accuracy. Figure 6(a) displays a forescatter electron (FSE) image showing the EBSD point analyses on three different constituents, i.e., Nb-rich irregular-shaped Laves phase, Nb-rich MC carbide, and matrix (designated by points (b)-(d), respectively). Figures 6(b-d) shows the Kikuchi pattern of points designated in Figure 6(a), where they are successfully indexed by the AZtec software as $MgZn_2$ (C14 Laves phase), NbC, and Ni-matrix. The Kikuchi patterns indexing using EBSD on the secondary phase constituents in the interdendritic region further confirms that they are Laves phase and Nb-rich MC carbide.

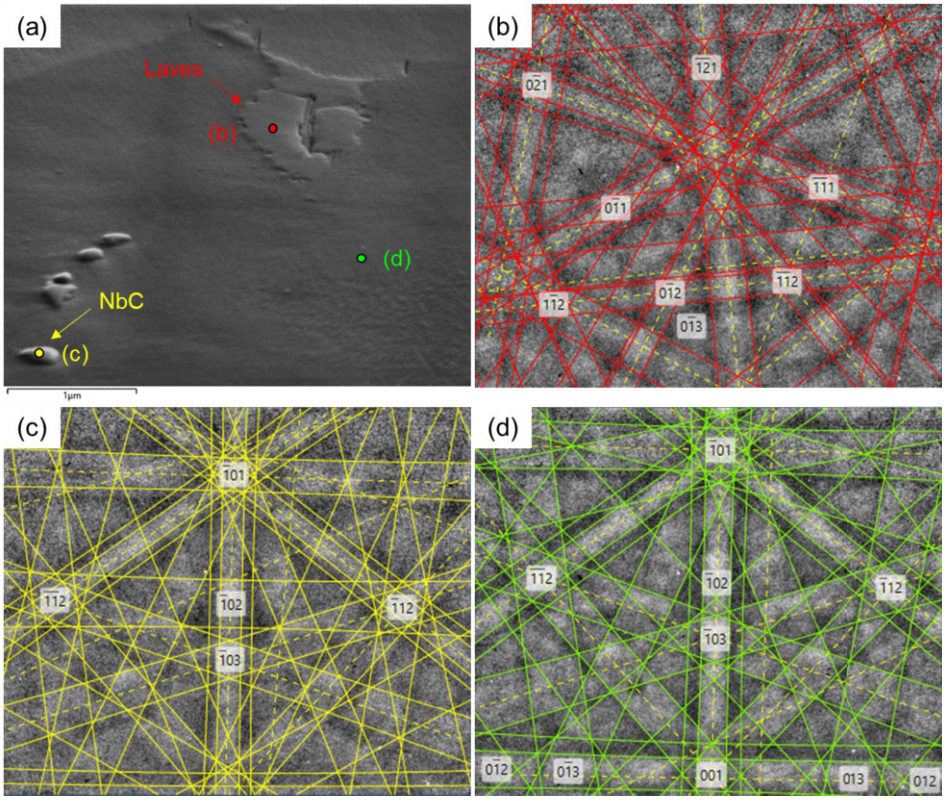

Figure 6. EBSD point analysis of FZ of as-welded G27 that shows: (a) FSE image of Laves phase and Nb-rich MC particle, (b-d) Kikuchi patterns indexed by Aztec EBSD software from the points designated in (a). as C14 Laves phase, NbC, and matrix, respectively.

3.4. Microstructural evolution during weld fusion zone solidification

The initiation of solidification commences with the forming of primary γ dendrites through the reaction of L → γ. As the dendrites grow, solute elements possessing equilibrium partition coefficients less than unity are rejected into the interdendritic liquid. When the solubility limit of these solute elements within the interdendritic liquid is exceeded, secondary solidification phase constituents form from the liquid phase. During the growth of primary γ dendrites, MC-type carbide-forming elements such as Nb, Mo, Ti, and C continuously accumulate within the interdendritic liquid due to microsegregation. This accumulation ultimately results in the formation of MC-type carbides, which the reaction is most likely to occur through a monovariant eutectic reaction of L→ γ + MC over a temperature range.

The formation of MC-type carbides from the liquid phase leads to a substantial depletion of available carbon within the interdendritic liquid. Subsequently, as the cooling process progresses, the residual interdendritic liquid remains continuously enriched with Nb, resulting in the formation of the Laves phase through a reaction L → γ + MC over a temperature range, owing to the supersaturation of Nb.

The Laves phase within the FZ of the as-welded G27 necessitates meticulous consideration, as it is widely acknowledged that this phase has deleterious impacts on the mechanical properties of Ni-based superalloys. Notably, Schirra et al. [11] observed that the Laves phase in Alloy 718 exhibits a feeble interface with the γ matrix, rendering it susceptible to acting as a preferential site for initiating and propagating cracks due to its inherent brittleness. In addition, James [12] reported that the weldment of Alloy 718, which still contains a substantial Laves phase content, displays a higher crack propagation rate at elevated temperatures in contrast to weldments in which the Laves phase has been entirely removed. Hence, the present study highlights the critical necessity of formulating a suitable post-weld heat treatment (PWHT) aimed at eliminating or lessening the presence of the Laves phase within the weld FZ of G27 to optimize the properties and reliability of the G27 weldment.

4. Summary

The influence of pulsed laser beam welding (LBW) parameters on the weld geometry and imperfections of a G27 was studied by a statistical DOE, and the microstructures of the weld fusion zone (FZ) of the pulsed laser beam-welded G27 were characterized. The following can be summarized from the results:

- No cracks are found in the FZ and HAZ of all welded samples.
- Among the 19 DOE runs carried out, only six met the Wm requirement of 1.5 mm, whereas all DOE runs produced welds with root excess weld metal and average pore diameter below the maximum acceptable limit as stipulated in AWS D17.1 M:2010 for aerospace applications.
- The pulse factor significantly influenced all the responses, i.e., minimum weld width (Wm), root excess weld metal, and average pore diameter, whereas welding travel speed significantly influenced Wm and root excess weld metal. Power and interaction between pulse frequency*pulse factor were statistically significant in influencing the root excess weld metal and average pore diameter, respectively. The pulse frequency and interactions between power*travel speed,

power*pulse factor, power*pulse frequency, travel speed*pulse factor, and travel speed*pulse frequency did not significantly influence any response.

- Microsegregation pattern in the weld FZ leads to the formation of major secondary phase constituents that are identified as Nb-rich MC carbides and Nb-rich Laves phase.
- The presence of brittle Laves phase requires careful consideration when developing suitable post-weld heat treatment of G27.

5. Acknowledgment

This study is based on the research conducted within the FEAST project (Weld Feasibility Heat Treatment Studies of New Superalloys, registration number 2019-02787) funded by the Swedish funding agency VINNOVA. We extend our profound gratitude for the invaluable assistance and insights provided by Dr. Ceena Joseph and Mr. Bengt Pettersson from GKN Aerospace AB and Mr. Fredrik Olofsson at Brogren Industries AB. Furthermore, we express our gratitude to Carpenter Technology Corporation for their material supply. We extend a special acknowledgment to Mattias Igestrand of University West for his immense help performing the pulse LBW operations.

References

[1] K.A. Heck, N. Zhou, S.J. Kernion, D. Rickert, F. Van Weereld, A New Co-free Ni-Based Alloy for Gas Turbine and Exhaust Valve Applications, Superalloys 2020, Springer2020, pp. 142-152. https://doi.org/10.1007/978-3-030-51834-9_14.

[2] A. Khan, P. Hilton, J. Blackburn, C. Allen, Meeting weld quality criteria when laser welding Ni-based alloy 718, International Congress on Applications of Lasers & Electro-Optics, Laser Institute of America, 2012, pp. 549-557. https://doi.org/10.2351/1.5062506.

[3] P. Alvarez, L. Vázquez, N. Ruiz, P. Rodríguez, A. Magaña, A. Niklas, F. Santos, Comparison of hot cracking susceptibility of TIG and laser beam welded alloy 718 by varestraint testing, Metals 9(9) (2019) 985. https://doi.org/10.3390/met9090985

[4] L. Eriksson, E. Johansson, N. Kettaneh-Wold, C. Wikström, S. Wold, Design of experiments, Principles and Applications, Learn ways AB, Stockholm (2000).

[5] J. DuPont, A. Marder, M. Notis, C. Robino, Solidification of Nb-bearing superalloys: Part II. Pseudoternary solidification surfaces, Metallurgical and Materials Transactions A 29(11) (1998) 2797-2806. https://doi.org/10.1007/s11661-998-0319-3

[6] D.F. Paulonis, J.M. Oblak, D.S. Duvall, Precipitation in Nickel-base Alloy 718, Pratt and Whitney Aircraft, Middletown, Conn., 1969.

[7] G. Asala, J. Andersson, O.A. Ojo, Precipitation behavior of γ' precipitates in the fusion zone of TIG welded ATI 718Plus®, The International Journal of Advanced Manufacturing Technology 87(9) (2016) 2721-2729. https://doi.org/10.1007/s00170-016-8642-0

[8] O. Ojo, N. Richards, M. Chaturvedi, Study of the fusion zone and heat-affected zone microstructures in tungsten inert gas-welded INCONEL 738LC superalloy, Metallurgical and materials transactions A 37(2) (2006) 421-433. https://doi.org/10.1007/s11661-006-0013-2

[9] G. Knorovsky, M. Cieslak, T. Headley, A. Romig, W. Hammetter, Inconel 718: a solidification diagram, Metallurgical transactions A 20(10) (1989) 2149-2158. https://doi.org/10.1007/BF02650300

[10] R.G. Thompson, D.E. Mayo, B. Radhakrishnan, The relationship between carbon content, microstructure, and intergranular liquation cracking in cast nickel alloy 718, Metallurgical Transactions A 22 (1991) 557-567 %@ 0360-2133. https://doi.org/10.1007/BF02656823

[11] J.J. Schirra, R.H. Caless, R.W. Hatala, The effect of Laves phase on the mechanical properties of wrought and cast+ HIP Inconel 718, Superalloys 718(625) (1991) 375-388. https://doi.org/10.7449/1991/SUPERALLOYS_1991_375_388

[12] L.A. James, Fatigue-crack growth in Inconel 718 weldments at elevated temperatures, Welding Journal Research Supplement 57(1) (1978) 17s-23s.